SCIENTIFIC REPORTS

OPEN

MoS_2@rGO Nanoflakes as High Performance Anode Materials in Sodium Ion Batteries

Received: 7 March 2017
Accepted: 11 July 2017
Published online: 11 August 2017

Ruxing Wang[1], Shu Gao[1], Kangli Wang[2], Min Zhou[2], Shijie Cheng[2] & Kai Jiang[1,2]

A simple one-pot hydrothermal method is developed for fabrication of MoS_2@rGO nanoflakes using the economical MoO_3 as the molybdenum source. Benefiting from the unique nanoarchitecture, high MoS_2 loading (90.3 wt%) and the expanded interlayer spacing, the as-prepared MoS_2@rGO nanoflakes exhibit greatly enhanced sodium storage performances including a high reversible specific capacity of 441 mAh g^{-1} at a current density of 0.2 A g^{-1}, high rate capability, and excellent capacity retention of 93.2% after 300 cycles.

Rechargeable sodium ion batteries (SIBs) are seen as promising options for large scale energy storage systems because of the natural abundance of sodium and lower production cost[1–6]. Na and Li elements share many similar physical and chemical properties, which makes the strategies applied in lithium ion batteries (LIBs) valuable references to develop SIBs[7–9]. However, the large radius of Na ion and sluggish transport kinetics limit the stability and rate performance in most electrode materials and thus hinder the development of SIBs[10–14].

Molybdenum disulfide (MoS_2), with a well-defined lamellar structure similar to graphite, has been actively studied as anode material for both LIBs and SIBs[15–20]. Although the discharge (Na intercalation) potential is slightly higher than other anode materials like carbon and metal oxides, MoS_2 is particularly attractive as a high capacity sodium host (theoretical capacity ~670 mA h g^{-1}, based on 4 mol of Na^+ insertion), due to its dichalcogenide structure and large interlayer spacing. However, because of its high surface energy and interlayer van der Waals attractions, the two-dimensional (2D) layered structure is thermally unstable, and has a trend to restack irreversibly during the cycling process, leading rapid capacity fading and poor rate performance[21–24]. This phenomenon is especially severe in Na^+ storage because Na ions are about 55% larger in radius than Li ions[8, 11]. Previous studies have revealed that when MoS_2 is cycled to very low potential (0 V versus Na/Na^+) to achieve high capacity for SIBs, Mo metal nanoparticles are formed within a Na_2S matrix, and subsequent electrochemical cycling operates as a sodium–sulfur redox couple. It indicates that the parent crystalline atomic structure of MoS_2 is completely destroyed and does not reform after the Na is removed, resulting in poor cycling stability especially at high rates[12, 25–27]. Cycled in a limited voltage region (between 0.5–2.6 V versus Na/Na^+) without destroying the 2D atomic layered structure of MoS_2 has been proved to be an effective way to improve the cyclability, but the achieved capacity is much lower than the target[28, 29].

To enhance the structure stability of MoS_2, various strategies have been proposed and can be mainly divided into two categories: designing nanoarchitecture and incorporating with carbonaceous materials[15–17, 30]. Different types of nanoscale architectures have been suggested, such as nanotubes, nanoboxes, nanoflowers and hollow nanospheres, which are expected to improve the reversible capacity of MoS_2 by alleviating the restacking of the nanosheets. For example, Hu *et al.* have fabricated MoS_2 nanoflowers with expanded interlayers, which deliver a reversible capacity of 350 $mAhg^{-1}$ at a limited voltage region (0.4–3 V vs. Na/Na+)[29]. Su *et al.* reported an ultrathin MoS_2 exfoliated nanosheets, which exhibited a high initial discharge capacity of 998 mAh g^{-1} while after 100 cycles the remained discharge capacity is just 386 mAh g^{-1}[10]. The cycle stability of nanoarchitecture MoS_2 is still far from an ideal and exhibits an obvious capacity decay from the very beginning. The poor performance may be attributed to the large volume change during cycle which tends to severely damage the carefully designed nanostructure. Incorporating with carbonaceous materials (e.g. graphene, carbon nanotubes, and carbon coating)

[1]State Key Laboratory of Materials Processing and Die & Mould Technology, School of Materials Science and Engineering, Huazhong University of Science and Technology, Wuhan, Hubei, 430074, China. [2]State Key Laboratory of Advanced Electromagnetic Engineering and Technology, School of Electrical and Electronic Engineering, Huazhong University of Science and Technology, Wuhan, Hubei, 430074, China. Ruxing Wang and Shu Gao contributed equally to this work. Correspondence and requests for materials should be addressed to K.W. (email: klwang@hust.edu.cn) or K.J. (email: kjiang@hust.edu.cn)

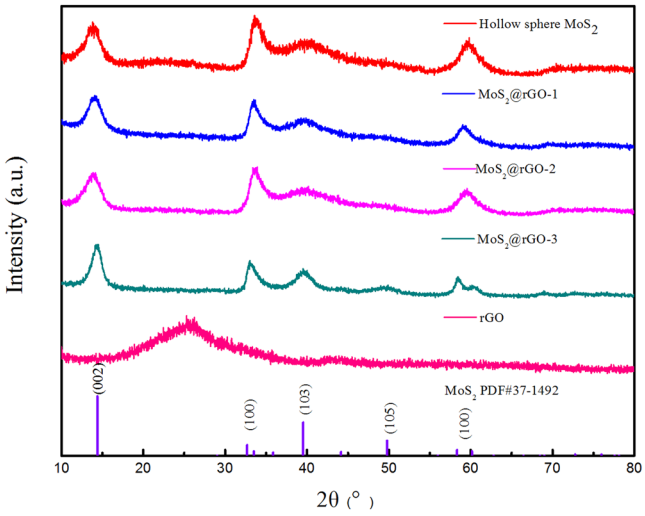

Figure 1. XRD patterns of the prepared rGO, pristine MoS_2, and MoS_2@rGO composites.

is another effective approach. Graphene oxide (GO) with a well-defined lamellar structure similarity to MoS_2 may sever as an excellent carbon host to modify structural stability, improve the electronic conductivity and trigger enhanced reaction kinetics of MoS_2. Qin *et al.* prepared MoS_2-reduced graphene oxide (rGO) composites via a facile microwave assisted method, achieving a stable reversible capacity of 305 mAh g^{-1} at 100 mA g^{-1}. However, the remained capacity was only 218 mAh g^{-1} after 50 cycles[31]. Xie *et al.* prepared MoS_2/rGO nanocomposites with intimate two-dimensional heterointerfaces by hydrothermal method, the composite exhibits much higher initial capacity of 702 mAh g^{-1} at a current density of 20 mA g^{-1}, but the capacity retention is only 49% after 100 cycles[21]. It is assumed that a suitable rGO host can optimize the electrochemical performance by improve the electron and ion transfer ability of the composite and buffer the large volume change during cycle, but in most cases the synthesis processes are relatively complicated and the molybdenum sources are rather expensive. Therefore, it is desirable to develop a MoS_2 anode with both high capacity and long cycle life in an economical way.

Herein, we report a facile one-pot hydrothermal strategy to prepare the MoS_2@rGO composites using an economical molybdenum source of MoO_3. By controlling the concentration of aqueous rGO solution in hydrothermal treatment and engineering the ionic strength of precursors, three-dimensional (3D) architectures constructed of MoS_2/rGO nanoflake is developed. The prepared MoS_2@rGO composites with high loading of MoS_2 exhibit excellent cycle stability and rate performance, making the synthesized MoS_2@rGO a promising anode material for SIBs.

Results and Discussion

X-ray diffraction spectrometry (XRD) is used to investigate the crystalline phases of the as prepared MoS_2 and MoS_2@rGO composites (the composites with different weight ratios of MoS_2 are named as MoS2@rGO-1,2,3). As shown in Fig. 1, all of the identified peaks belong to the MoS_2 (JCPDS 37–1492), demonstrating that MoS_2 is successfully synthesized. Compared to the pristine MoS_2, the MoS_2@rGO composites exhibit broadened and less prominent peaks at (002) and (103), suggesting the formation of smaller MoS_2 crystallite. In addition, the interlayer spacing (d_{002} value) of the MoS_2@rGO composites is calculated to be 0.64 nm, which is larger than that of the pristine MoS_2 (0.61 nm), implying the expansion in the (002) interlayer of MoS_2. The expanded interlayer of MoS_2 can lower the energy barrier of Na^+ intercalation and facilitate Na^+ diffusion[32,33]. Meanwhile, the (002) characteristic broad peak of rGO at about 26° is not observed in the MoS_2@rGO composites, suggesting the fine distribution and exfoliation of rGO sheets which is beneficial for electronic conducting and high mass loading of MoS_2. X-ray photoelectron spectroscopy (XPS) measurements are conducted to analyze the composition and chemical states of MoS_2@rGO composites. The two peaks at 233.0 and 229.9 eV in the inset graph of Fig. 2a are assigned to the binding energies of the Mo $3d_{3/2}$ and Mo $3d_{5/2}$ of Mo^{4+}. The spectra of S 2p in Fig. S1 (see in supporting information) reveals two peaks at 163.9 and 162.7 eV corresponding to S $2p_{1/2}$ and S $2p_{3/2}$, indicating the valence of S is −2. In the meantime, the C1s peak appearing at 285.0 eV (Fig. S1) is related to the binding energy of the sp^2 C-C bonds of rGO. Raman spectrum of the MoS_2@rGO-2 composite is also shown in Fig. 2b. The D and G band at 1341 and 1574 cm^{-1} are the feature peaks of rGO. The peaks at 376.1 and 402.0 cm^{-1} are attributed to the planar (E^1_{2g}) and out-of-plane (A_{1g}) vibrations, respectively, indicating the few stack layered structure of MoS_2 in rGO[34–36]. The Raman spectra of different MoS_2@rGO composites are shown in Fig. S2 (ESI). The intensity ratios between D band and G band (ID/IG) of the composites are calculate to be 1.36 (MoS_2@rGO-1), 1.42 (MoS_2@rGO-2) and 1.43 (MoS_2@rGO-3). As is known, the intensity ratio between D band and G band (ID/IG) is an important parameter to evaluate the rGO composites, the higher the ID/IG ratio, the stronger the disorder degree will be. For electrode materials, a higher ID/IG ratio is beneficial for electronic conducting and electrolyte penetration.

The MoS_2 loading and surface area of the MoS_2@rGO composites are characterized by the TGA measurement and N_2 adsorption/desorption isotherm analysis, respectively, which are summarized in Table S1. The contents of MoS_2 in the composites are determined to be 94.7 wt% (MoS_2@rGO-1), 90.3 wt% (MoS_2@rGO-2), and 81.4 wt% (MoS_2@rGO-3). Corresponding thermogravimetric curves of MoS_2@rGO composites are shown in Fig. S3. As

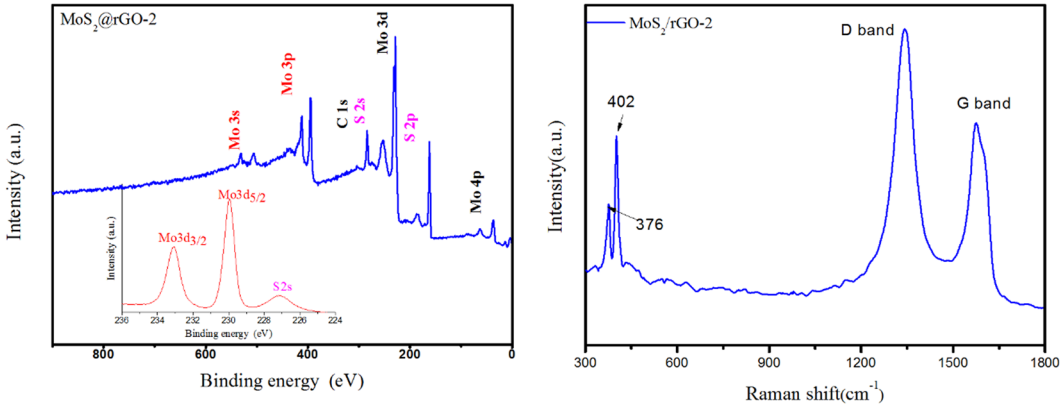

Figure 2. (**a**) XPS spectrum of MoS_2@rGO-2 composite and the peaks of Mo 3d in the inset graph, (**b**) Raman spectrum of the MoS_2@rGO-2.

seen in Table S1, hollow sphere MoS_2 possess a relative small BET specific surface area of 8.6 $m^2 g^{-1}$. When compositing with rGO (BET specific surface area is 106.3 $m^2 g^{-1}$), the BET surface area of the composites increase to 18.9 $m^2 g^{-1}$ (MoS_2@rGO-1), 26.3 $m^2 g^{-1}$ (MoS_2@rGO-2), and 37.2 $m^2 g^{-1}$ (MoS_2@rGO-3). The increased BET surface area may modify the electrode-electrolyte interface and provides fast Na ion diffusion channel. However, the specific capacity of composites may decrease because rGO serves merely as a buffer and conductive skeleton rather than the accommodation of Na ion. Raising the proportion of rGO in the composite is beneficial for the enhanced conductivity but unfavorable for the specific capacity.

Microstructures of the pristine MoS_2 and the MoS_2@rGO composites are further observed by scanning electron microscopy (SEM) and transmission electron microscopy (TEM). The SEM images of products obtained with different concentration of rGO solution are also shown in Fig. 3a–d. As seen, the pristine MoS_2 in Fig. 3a consists of hollow spherical particles with an average diameter of about 1 um. When rGO is introduced into MoS_2, hollow spherical structure is effectively inhibited and composite with nanoflake morphology is shown (Fig. 3b). But bulk MoS_2 still exists for the low ratio of rGO. As the content of rGO increasing, the uniformly distributed MoS_2 nanoflakes with planar width of 200 nm on rGO sheets are observed in Fig. 3c and d for MoS_2@rGO-2 and 3. Composites with different rGO contents show significant changes from crumpled and aggregated morphologies to rather flat surfaces with uniformly distribution. The TEM images of MoS_2@rGO-2 in Fig. 3e and f further verify the lamellar structure of MoS_2 with an interlayer spacing of 0.64 nm, which agrees with the d_{002} of hexagonal MoS_2 obtained from XRD results. The few-layer MoS_2 nanoflakes are vertically grown and embedded in the rGO nanosheets, providing sufficient open channels for sodium ion intercalation. Such unique architecture not only enhances the electrical conductivity and stability of active materials, but also favors an increase in the high loading of MoS_2 in the composites.

The dramatically different microstructures of the pristine MoS_2 and MoS_2@rGO may attribute to the unique synthesis mechanism as displayed in Fig. 4. The formation of pristine MoS_2 hollow spheres can be explained by Kirkendall effect: First, the MoO_3 is reduced by $NH_2OH{\cdot}HCl$ to form MoO_2 on the surface ($2MoO_3 + 2NH_2OH{\cdot}HCl \rightarrow 2MoO_2 + N_2O + 2HCl + 3H_2O$). In the meantime, NH_2CSNH_2 is hydrolyzed to form H_2S ($CS(NH_2)_2 + 2H_2O \rightarrow CO_2 + 2NH_3 + H_2S$). Then, surface MoO_2 reacts with H_2S to form MoS_2 shell outside the MoO_2-MoO_3 which serves as the moving boundary in the subsequent reaction. At the last, inner MoO_3 is reduced to MoO_2 then react with HCl to form Mo^{4+}, which transfer along the formed MoS_2 boundary and reacting with H_2S to form MoS_2 hollow spherical eventually. For MoS_2@rGO composite, the addition of positive-charged NH_4^+ could screen the electrostatic repulsion of GO colloids and the MoO_3 powders can be uniformly adsorbed onto GO sheets. Owing to the oxygenated functional groups acted as nucleation sites, the MoS_2 grows gradually perpendicular to the GO skeleton surface and forms nanoflakes as the gradual reaction proceeding during hydrothermal treatment. The unique vertical aligned MoS_2 nanoflake could maximize the MoS_2 loading in composites (90.3 wt%) which is much higher than those shown in previous reports.

The electrochemical properties of MoS_2 and MoS_2@rGO composite are characterized by CV and galvanostatic charge-discharge cycling. Figure 5a show the initial four cycles of the MoS_2@rGO composite in the range of 0–3 V vs. Na^+/Na at a scan rate of 0.1 mV s^{-1}. In the first cycle, three reduction peaks in the sodiation process are observed. The reduction peak at 0.81 Vs. Na^+/Na is assigned to the Na^+ insertion into MoS_2 to form Na_xMoS_2 ($x < 2$). The following reduction peak at 0.53 V vs. Na^+/Na is attributed to the further insertion of Na^+ and at the same time with the formation of solid electrolyte interphase (SEI) layer. The broad peak at 0.1 V vs. Na^+/Na is related to the conversion of MoS_2 to form metallic (Mo) embedded in an amorphous Na_2S matrix. A broad anodic peak observed in the first charging process at about 1.8 V corresponds to the oxidation of the Mo and Na_2S to MoS_2. In brief, the sodiation/desodiation of the MoS_2@rGO composites appears to be based on a two-step reaction process, including an initial insertion process described by $MoS_2 + x\text{Na} \leftrightarrow \text{Na}xMoS_2$ ($x < 2$) and the following conversion reaction that MoS_2 converts into Mo and Na_2S described by $Na_xMoS_2 + (4 - x)\ \text{Na} \leftrightarrow \text{Mo} + 2Na_2S$. The CV curves exhibit no significant variation during the following three cycles, demonstrating the high stability and reversibility of the electrode. The *ex-situ* XRD result (Fig. S4) also identify the compositional changes of the MoS_2@rGO composites during the first charge/discharge, which is consistent with the CV. The charge-discharge

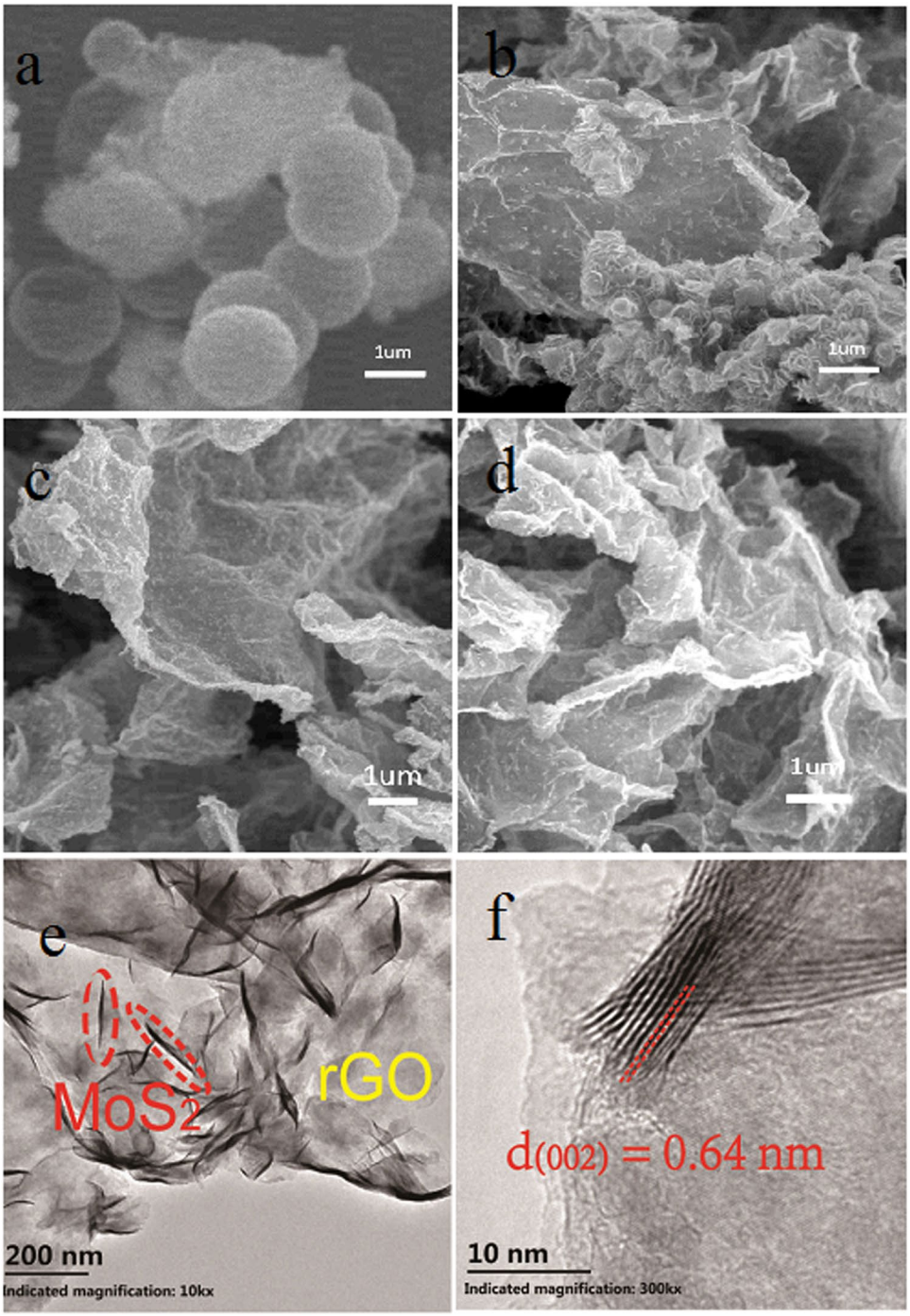

Figure 3. SEM images of the (**a**) pristineMoS_2 and (**b**–**d**) MoS_2@rGO2 composites, (**e**,**f**) the TEM images of MoS_2 nanoflakes on rGO sheets of MoS_2@rGO-2.

curves of the MoS_2@rGO composite at a constant current density of 0.2 A g^{-1} are shown in Fig. 5b. The initial discharge curves consist of three plateaus at 1.5–0.8 V, 0.75–0.4 V and 0.4–0.01 V vs. Na^+/Na, respectively, which are consistent with the CV results. In the subsequent discharge, the plateaus are disappeared and replaced by a long slopes curve as a result of the conversion reaction mechanism, which is in good agreement with previous reports.

The cycling stability of the pristine MoS_2 and MoS_2@rGO composites were further evaluated at 0.2 A g^{-1} as shown in Fig. 6a. The initial discharge capacity of the pristine MoS_2 is about 470 mAh g^{-1}, but drops quickly to 105 mAh g^{-1} after 100 cycles, primarily due to the serious structural collapse and aggregation of the hollow MoS_2 spheres during the charging/discharging process. On the contrary, MoS_2@rGO-1,2,3 composites deliver high initial discharge capacities of 521, 543 and 610 mAh g^{-1} with a corresponding first cycle coulombic efficiency of 74.6%, 66.9% and 67.4%, respectively. After the first cycle, the discharge capacity of the composites increased slowly until a stable range of 381, 441 and 412 mAh g^{-1} (50th cycle). MoS_2@rGO-2 reveals the largest reversible

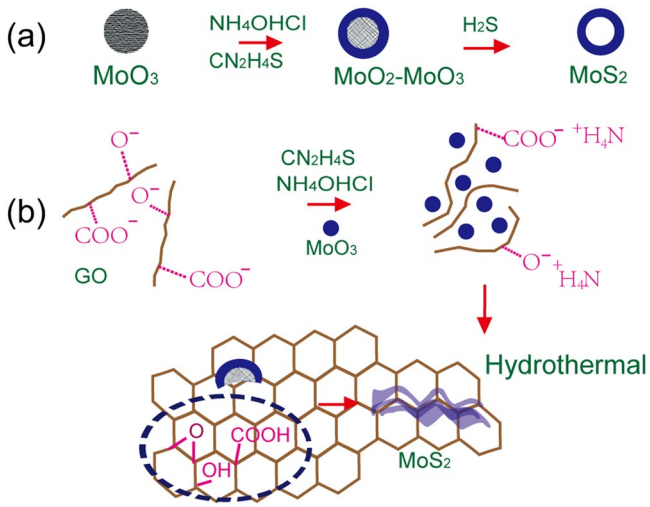

Figure 4. The synthesis of the (**a**) pristine MoS_2 and (**b**) MoS_2@rGO composites.

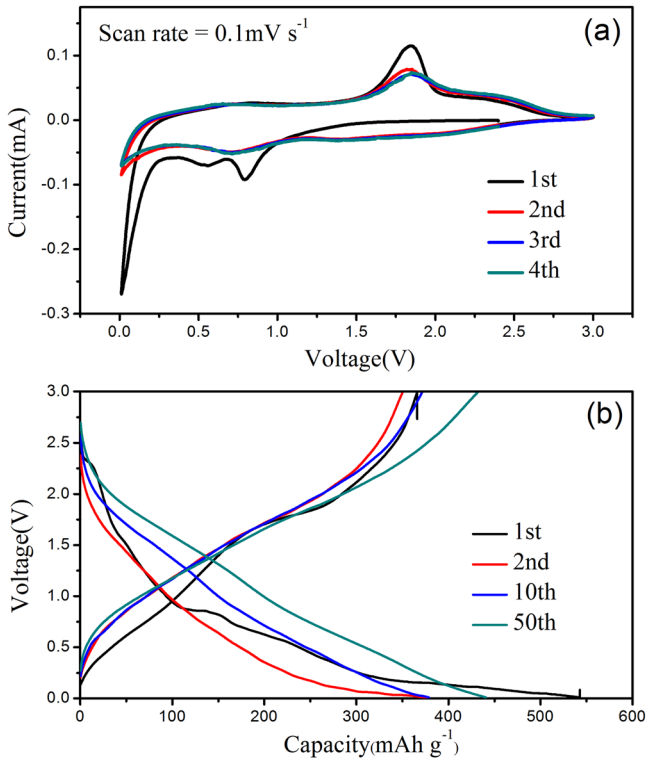

Figure 5. (**a**) CV curves at a potential sweep rate of 0.1 mV $s^{-1}$and (**b**) discharge profiles of the MoS_2@rGO-2 composite at 0.2 A g^{-1}.

specific discharge capacity. The coulombic efficiency of MoS_2@rGO composites rise up to 99% rapidly in the initial few cycles (Fig. S5). Moreover, the reversible capacities remain 382, 442, 410 mAh g^{-1} after 100 cycles, nearly 4 times higher than that of the pristine MoS_2. In the meantime, the electrochemical performance of rGO at a current density of 0.2 A g^{-1} has been evaluated as shown in Fig. S6. The initial discharge capacity of the rGO is about 500 mAh g^{-1}, with a low first cycle coulombic efficiency of 13%. The specific discharge capacity drops quickly to 83 mAh g^{-1} at the second cycle, after 100 extended cycles, a low reversible capacity of 54 mA h g^{-1} is maintained. This result further confirms that the specific capacity of MoS_2@rGO composites mainly come from the MoS_2. In conclusion, the excellent cycle stability of the MoS_2@rGO composite may be the results of well developed 3D interconnected nanoflakes structure which benefits fast ion intercalation and provides structural stability. Note that after 300 extended cycles in Fig. S7, a high reversible capacity of 411 mA h g^{-1} is still maintained in the MoS_2@rGO-2, with a capacity retention of 93.2% based on the reversible capacities of the 50th cycles, corresponding to a capacity decay of 0.027% per cycle. This can be attributed to the higher MoS_2 loading and more

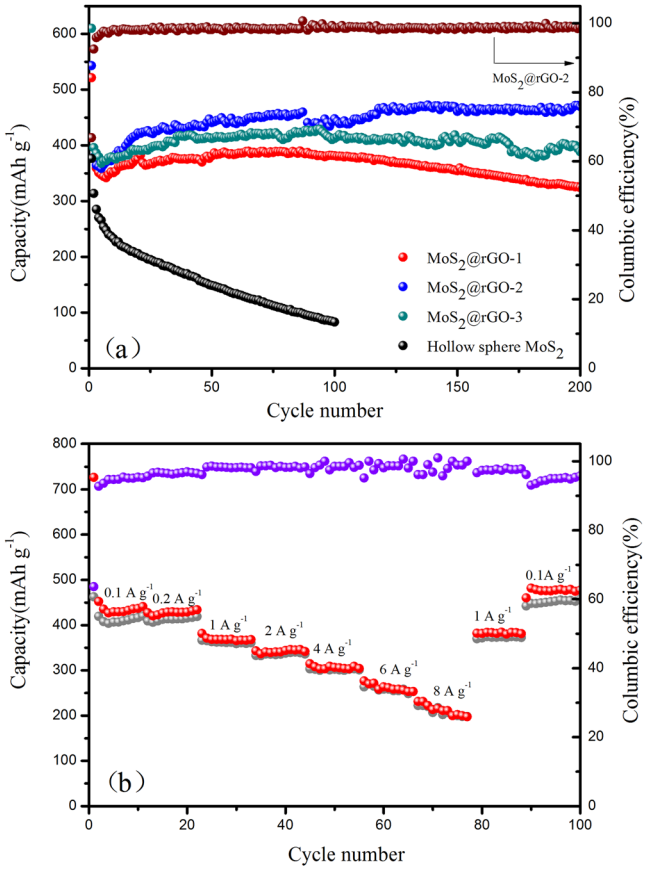

Figure 6. (**a**) The cycle performance of the pristine MoS_2, MoS_2/rGO-1,2,3 at 0.2 A g^{-1}, (**b**) the rate performance of the MoS_2@rGO-2 from 0.1 to 8 A g^{-1}.

homogeneous dispersion which could effectively inhibit the aggregation of MoS_2 and accommodate the volume change to maintain the physical stability.

Furthermore, the MoS_2@rGO-2 also demonstrates a very impressive performance at high current density which is shown in Fig. 6b. The reversible discharge capacities of 435, 427, 369, 337, 314 and 258 mAh g^{-1} are obtained at 0.1, 0.2, 1, 2, 4 and 6 A g^{-1}, respectively. Even the current density increased by 80 times to as high as 8 A g^{-1}, a capacity of 211 mAh g^{-1} is still obtained, with a capacity retention of 48.5%. As the current density decreases back to 0.1 A g^{-1}, the reversible capacity switches back with a high value of 477 mAh g^{-1} and keeps stable in the following cycles, indicating an excellent high rate cyclability of the MoS_2@rGO-2. Apparently, fast kinetics of MoS_2@rGO are due to the enhanced electrical conductivity combined with an ideal nanoscale architecture consisting of interconnected nanoflakes with short ion diffusion path lengths and good electrolyte accessibility, which is further confirmed by the electrochemical impedance spectroscopy (EIS) measurements. The Nyquist plots of the MoS_2 and MoS_2@rGO nanoflakes after different cycles (30^{th} and 50^{th}) are displayed in Fig. 7 and Fig. S8 and the fitting results are listed in Table 1. The SEI resistance (R_{SEI}) and charge transfer resistance (R_{ct}) of the pristine MoS_2 increase dramatically during cycling, implying the poor structural stability and sluggish kinetics. For the MoS_2@rGO nanoflakes, R_S and R_{ct} are much smaller than that of the MoS_2, and keep almost constant during cycling, indicating a thinner and more stable SEI film favoring rapid Na+ insertion/extraction and fast charge transfer at the electrode/electrolyte interface, which in part explains the high discharge capacity and good rate capability of MoS_2@rGO nanoflakes that have been observed.

Conclusion

In summary, the ultra-stable MoS_2@rGO composites as anode materials in SIBs were synthesized via a facile hydrothermal method. Owing to the oxygen functional groups of rGO acted as the nucleation sites, few-layered MoS_2 nanoflakes are vertically grown and embedded in the rGO nanosheets, which exhibits high specific capacity, outstanding cycle stability and rate capability. The greatly enhanced electrochemical performance of the MoS_2@rGO nanoflakes can be mainly attributed to the synergistic effect of its unique structural features and high loading of active materials, which not only enhances the electrical conductivity and create more electrochemically active sites, but also alleviate the huge inherent volume change of MoS_2. Furthermore, the expanded interlayer distance of the MoS_2 nanosheets benefits fast ion intercalation and provides structural stability, leading to high rate capability and long term cyclability. In addition, this synthesis route with the economical metal oxides as the sources of metal elements may be suitable for the fabrication of other high-loading metal sulfides@rGO composites with outstanding performance in SIBs.

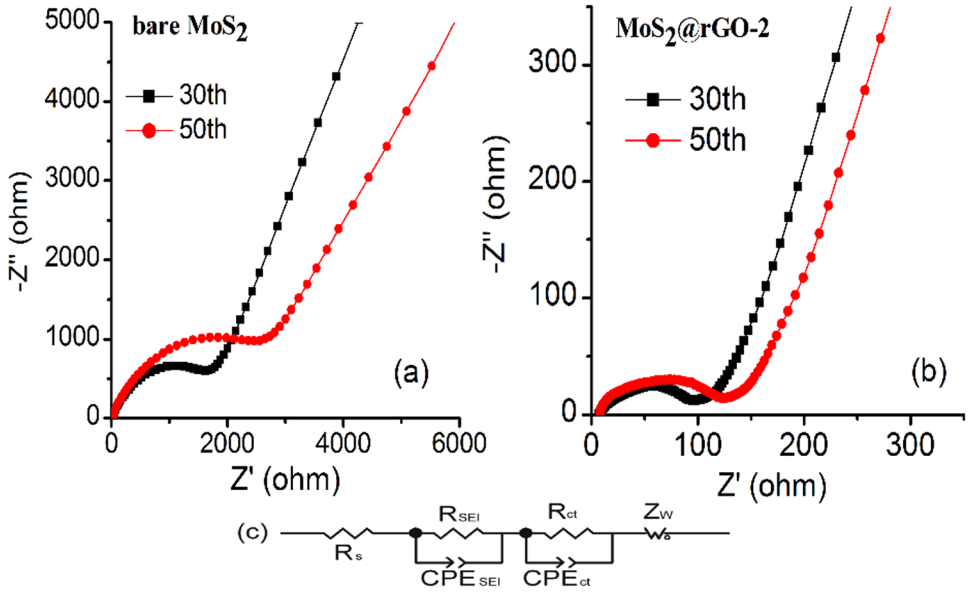

Figure 7. The nyquist plots of the (**a**) pristine MoS_2, (**b**) MoS_2@rGO-2, and (**c**) the equivalent circuit for EIS fitting.

Cycle number	R_s (Ω)		R_{SEI} (Ω)		R_{ct} (Ω)	
	30th	50th	30th	50th	30th	50th
MoS_2	20.0	11.1	83.3	2714	1726	6515
MoS_2@rGO-1	8.8	11.6	10.7	26.7	166.2	247.9
MoS_2@rGO-2	8.1	6.9	10.7	22.9	67.1	79.5
MoS_2@rGO-3	5.8	6.2	14.3	16.8	45.3	63.3

Table 1. The fitting results of electrochemical impedance spectroscopy of the pristine MoS_2 and the MoS_2@rGO-1,2,3 composite for the 30th and 50th cycles.

Methods

Material synthesis. GO was synthesized in a modified Hummer's method using the commercial graphite as the original material[37]. MoS_2@rGO is synthesized by hydrothermal method as follows: 1.0 g MoO_3, 1.5 g thiocarbamide and 1.5 g NH_4OHCl were uniformly mixed in 40 ml of DI water via vigorous magnetic stirring. 40 ml of GO suspensions with different concentrations (2, 5, 10 mg ml^{-1}) were added to the precursor suspension dropwise and kept stirring vigorously for 20 min. The precursor was then transferred to an autoclave and subjected to a hydrothermal treatment at 180 °C for 48 h. The resultant was rinsed with DI water and ethanol repeatedly via filtration. The precipitate was dried in a vacuum oven at 80 °C overnight. Finally, the as-synthesized samples were annealed at 600 °C for 5 h in a N_2 atmosphere to reduce the oxygen functional groups of GO and improve the crystallinity of MoS_2 at the same time. The composites with different weight ratios of MoS_2 are named as MoS_2@rGO-1,2,3. The pristine MoS_2 was synthesized following the same hydrothermal route for comparison.

Material characterization. The morphology of the prepared composites was characterized by field-emission scanning electron microscopy (FESEM, SIRION200) and high-resolution transmission electron microscopy (HRTEM, JEOL2100). X-ray diffraction (XRD, PANalytical) equipped with a Cu-Kα1 radiation ($\lambda = 1.5406$ Å) was used to characterize the crystalline structure and interlayer spacing of MoS_2 in the 2θ range of 10–80°. The weight ratios of MoS_2 in composites were measured by the thermal gravity analysis (TGA, PerkinElmer TGA7) in the atmosphere of nitrogen and oxygen (80:20) at a heating rate of 10 °C min^{-1} in the temperature range of 30–600 °C. The N_2 adsorption-desorption isotherms were measured using an adsorption unit (Micromeritics, Tristar II 3020) to evaluate the Brunauer-Emmett-Teller (BET) surface area and pore size distribution. Prior to measurement, samples were degassed in a vacuum of 10^{-6} Torr at 150 °C for 12 h to remove the adsorbed moisture. X-ray photoelectron spectroscopy (XPS, Axis Ultra DLD) measurements were performed to analyze the element valence states of MoS_2@rGO composites with a monochromatic Al-Kα X-ray source. Raman spectra were recorded on a Renishaw Invia spectrometer using Ar^+ laser of 514.5 nm.

Electrochemical measurements. The MoS_2@rGO, Super P, the carboxymethyl cellulose and styrene butadiene rubber (1:1 by weight ratio) were mixed in a mortar at the weight ratio of 8:1:1 to form a homogenous paste and casted on the copper foil. The loading density of the active material was maintained at approximately 1.2 mg cm^{-2}. The electrode was dried in a vacuum oven at 120 °C for 12 h. The electrolyte was anhydrous solution

of 1 M $NaPF_6$ in ethylene carbonate and diethyl carbonate (1:1 in volume ratio). The sodium metal film was used as the counter electrode and the Celgard 2400 was used as the separator. The coin cells (CR2032) were assembled in an argon-filled glove box with the oxygen and moisture levels being less than 0.1 ppm. The galvanostatic charge-discharge tests (LAND, CT2001A) were tested in the potential range of 0.01–3.0 V at 25 °C. Cyclic voltammetry (CV) tests were performed at a scan rate of 0.1 mV s^{-1} in the voltage range of 0.01–3.0 V. Electrochemical impedance spectroscopy (EIS) measurements were performed at an AC amplitude of 5 mV in the frequency range of 10^5–10^{-2} Hz.

References

1. Zhou, M. *et al.* A sulfonated polyaniline with high density and high rate Na-storage performances as a flexible organic cathode for sodium ion batteries. *Chemical communications* **51**, 14354–14356, doi:10.1039/c5cc05654c (2015).
2. Yabuuchi, N., Kubota, K., Dahbi, M. & Komaba, S. Research development on sodium-ion batteries. *Chemical reviews* **114**, 11636–11682, doi:10.1021/cr500192f (2014).
3. Slater, M. D., Kim, D., Lee, E. & Johnson, C. S. Sodium-Ion Batteries. *Advanced Functional Materials* **23**, 947–958, doi:10.1002/adfm.201200691 (2013).
4. Li, W. *et al.* A high performance sulfur-doped disordered carbon anode for sodium ion batteries. *Energy Environ. Sci.* **8**, 2916–2921, doi:10.1039/c5ee01985k (2015).
5. Larcher, D. & Tarascon, J. M. Towards greener and more sustainable batteries for electrical energy storage. *Nature chemistry* **7**, 19–29, doi:10.1038/nchem.2085 (2015).
6. Dunn, B., Kamath, H. & Tarascon, J.-M. Electrical energy storage for the grid: a battery of choices. *Science* **334**, 928–935 (2011).
7. Ma, X., Luo, W., Yan, M., He, L. & Mai, L. *In situ* characterization of electrochemical processes in one dimensional nanomaterials for energy storages devices. *Nano Energy* **24**, 165–188, doi:10.1016/j.nanoen.2016.03.023 (2016).
8. Hong, S. Y. *et al.* Charge carriers in rechargeable batteries: Na ions vs. Li ions. *Energy & Environmental Science* **6**, 2067, doi:10.1039/c3ee40811f (2013).
9. Dahbi, M., Yabuuchi, N., Kubota, K., Tokiwa, K. & Komaba, S. Negative electrodes for Na-ion batteries. *Physical chemistry chemical physics: PCCP* **16**, 15007–15028, doi:10.1039/c4cp00826j (2014).
10. Su, D., Dou, S. & Wang, G. Ultrathin MoS2Nanosheets as Anode Materials for Sodium-Ion Batteries with Superior Performance. Advanced Energy Materials **5**, n/a-n/a, doi:10.1002/aenm.201401205 (2015).
11. Pan, H., Hu, Y.-S. & Chen, L. Room-temperature stationary sodium-ion batteries for large-scale electric energy storage. *Energy & Environmental Science* **6**, 2338, doi:10.1039/c3ee40847g (2013).
12. Liu, H. *et al.* Nitrogen-Rich Mesoporous Carbon as Anode Material for High-Performance Sodium-Ion Batteries. *ACS applied materials & interfaces* **7**, 27124–27130, doi:10.1021/acsami.5b06898 (2015).
13. Choi, S. H., Ko, Y. N., Lee, J.-K. & Kang, Y. C. 3D MoS2-Graphene Microspheres Consisting of Multiple Nanospheres with Superior Sodium Ion Storage Properties. *Advanced Functional Materials* **25**, 1780–1788, doi:10.1002/adfm.201402428 (2015).
14. Baggetto, L., Jumas, J. C., Gorka, J., Bridges, C. A. & Veith, G. M. Predictions of particle size and lattice diffusion pathway requirements for sodium-ion anodes using eta-Cu6Sn5 thin films as a model system. *Physical chemistry chemical physics: PCCP* **15**, 10885–10894, doi:10.1039/c3cp51657a (2013).
15. Zhu, C., Mu, X., van Aken, P. A., Yu, Y. & Maier, J. Single-layered ultrasmall nanoplates of MoS2 embedded in carbon nanofibers with excellent electrochemical performance for lithium and sodium storage. *Angewandte Chemie* **53**, 2152–2156, doi:10.1002/anie.201308354 (2014).
16. Wang, J. *et al.* An advanced MoS2/carbon anode for high-performance sodium-ion batteries. *Small* **11**, 473–481, doi:10.1002/smll.201401521 (2015).
17. Ramakrishna Matte, H. S. S. *et al.* MoS2 and WS2 Analogues of Graphene. *Angewandte Chemie* **122**, 4153–4156, doi:10.1002/ange.201000009 (2010).
18. Lacey, S. D. *et al.* Atomic force microscopy studies on molybdenum disulfide flakes as sodium-ion anodes. *Nano letters* **15**, 1018–1024, doi:10.1021/nl503871s (2015).
19. Feng, X. *et al.* Novel mixed-solvothermal synthesis of MoS2 nanosheets with controllable morphologies. *Crystal Research and Technology* **48**, 363–368, doi:10.1002/crat.201300003 (2013).
20. Du, G. *et al.* Superior stability and high capacity of restacked molybdenum disulfide as anode material for lithium ion batteries. *Chemical communications* **46**, 1106–1108, doi:10.1039/b920277c (2010).
21. Xie, X., Ao, Z., Su, D., Zhang, J. & Wang, G. MoS2/Graphene Composite Anodes with Enhanced Performance for Sodium-Ion Batteries: The Role of the Two-Dimensional Heterointerface. *Advanced Functional Materials* **25**, 1393–1403, doi:10.1002/adfm.201404078 (2015).
22. Liu, H. *et al.* Highly Ordered Mesoporous MoS2 with Expanded Spacing of the (002) Crystal Plane for Ultrafast Lithium Ion Storage. Advanced Energy. *Materials* **2**, 970–975, doi:10.1002/aenm.201200087 (2012).
23. Kong, D. *et al.* Rational design of MoS2@graphene nanocables: towards high performance electrode materials for lithium ion batteries. *Energy Environ. Sci.* **7**, 3320–3325, doi:10.1039/c4ee02211d (2014).
24. Zhou, J. *et al.* 2D space-confined synthesis of few-layer MoS2 anchored on carbon nanosheet for lithium-ion battery anode. *ACS nano* **9**, 3837–3848 (2015).
25. Stephenson, T., Li, Z., Olsen, B. & Mitlin, D. Lithium ion battery applications of molybdenum disulfide (MoS2) nanocomposites. *Energy Environ. Sci.* **7**, 209–231, doi:10.1039/c3ee42591f (2014).
26. Cook, J. B. *et al.* Mesoporous MoS2 as a Transition Metal Dichalcogenide Exhibiting Pseudocapacitive Li and Na-Ion Charge Storage. Advanced Energy Materials **6**, doi:10.1002/aenm.201501937 (2016).
27. Zhang, X., Li, X., Liang, J., Zhu, Y. & Qian, Y. Synthesis of MoS2 @C Nanotubes Via the Kirkendall Effect with Enhanced Electrochemical Performance for Lithium Ion and Sodium Ion Batteries. *Small* **12**, 2484–2491, doi:10.1002/smll.201600043 (2016).
28. Bang, G. S. *et al.* Effective liquid-phase exfoliation and sodium ion battery application of MoS2 nanosheets. *ACS applied materials & interfaces* **6**, 7084–7089, doi:10.1021/am4060222 (2014).
29. Hu, Z. *et al.* MoS2Nanoflowers with Expanded Interlayers as High-Performance Anodes for Sodium-Ion Batteries. *Angewandte Chemie* **126**, 13008–13012, doi:10.1002/ange.201407898 (2014).
30. Zhang, S. *et al.* Growth of ultrathin MoS(2) nanosheets with expanded spacing of (002) plane on carbon nanotubes for high-performance sodium-ion battery anodes. *ACS applied materials & interfaces* **6**, 21880–21885, doi:10.1021/am5061036 (2014).
31. Qin, W. *et al.* MoS2-reduced graphene oxide composites via microwave assisted synthesis for sodium ion battery anode with improved capacity and cycling performance. *Electrochimica Acta* **153**, 55–61, doi:10.1016/j.electacta.2014.11.034 (2015).
32. Rao, C. N. R. & Nag, A. Inorganic Analogues of Graphene. *European Journal of Inorganic Chemistry* **2010**, 4244–4250, doi:10.1002/ejic.201000408 (2010).
33. Zhou, X., Wan, L. J. & Guo, Y. G. Facile synthesis of MoS2@CMK-3 nanocomposite as an improved anode material for lithium-ion batteries. *Nanoscale* **4**, 5868–5871, doi:10.1039/c2nr31822a (2012).
34. Lee, C. *et al.* Anomalous lattice vibrations of single-and few-layer MoS2. *ACS nano* **4**, 2695–2700 (2010).

35. Hwang, H., Kim, H. & Cho, J. MoS2 nanoplates consisting of disordered graphene-like layers for high rate lithium battery anode materials. *Nano letters* **11**, 4826–4830 (2011).
36. Ryu, W. H., Jung, J. W., Park, K., Kim, S. J. & Kim, I. D. Vine-like MoS2 anode materials self-assembled from 1-D nanofibers for high capacity sodium rechargeable batteries. *Nanoscale* **6**, 10975–10981, doi:10.1039/c4nr02044h (2014).
37. Hong, Y., Wang, Z. & Jin, X. Sulfuric acid intercalated graphite oxide for graphene preparation. *Scientific reports* **3**, 3439, doi:10.1038/srep03439 (2013).

Acknowledgements

This work was supported by the Natural Science Foundation of China (Grant 51622703), the Fundamental Research Funds for the Central Universities (2017KFKJXX001, 2015ZDTD030) and the National Thousand Talents Program of China. The authors thank Analytical and Testing Center of HUST for XRD, SEM and FETEM measurements.

Author Contributions

K.J. and K.W. proposed and designed the work. R.W. and S.G. performed the experiments, R.W., S.G., K.W. and K.J. wrote and revised the manuscript. All authors analyzed and discussed the results.

Additional Information

Supplementary information accompanies this paper at doi:10.1038/s41598-017-08341-y

Competing Interests: The authors declare that they have no competing interests.

Publisher's note: Springer Nature remains neutral with regard to jurisdictional claims in published maps and institutional affiliations.